Ceramics International 45 (2019) 10733–10739

Contents lists available at ScienceDirect

Ceramics International

journal homepage: www.elsevier.com/locate/ceramint

Luminescent properties of stoichiometric Er:LiTaO_3 submicron particles synthesized by a modified solid-state combustion route

Xin Yang[b], Yunzhong Zhu[a,*], Decai Ma[a], Siwei Long[b], Zhihua Liu[b], Biao Wang[a,b,**]

[a] Sino French Institute of Nuclear Engineering and Technology, Sun Yat-sen University, Zhuhai, 519082, China
[b] School of Physics, Sun Yat-sen University, Guangzhou, 510275, China

A R T I C L E I N F O

Keywords:
Phosphor
Er:LiTaO_3
Submicron particles
Combustion
Luminescence

A B S T R A C T

Erbium-doped lithium tantalate submicron phosphor particles were produced by an efficient one-step solid-state combustion method. Well-crystallized products with uniform grain morphology were confirmed by X-ray diffraction and field-emission scanning electron microscopy. Thermogravimetric and differential thermal analysis were used to further analyze the combustion reaction process. In addition, down- and up-conversion luminescence (DCL, UCL) as well as the relationship between luminescence intensity and erbium doping level were revealed. The luminescence spectra for the UCL processes under different excitation intensities showed a remarkable three-photon absorption phenomenon in Er-doped system. These results demonstrate that the modified solid-state combustion method possesses practical value for large-scale synthesis of rare earth-doped submicron phosphors and has great potential for application in solid-state laser and display fields.

1. Introduction

Lithium tantalate (LiTaO_3, LT) is a photoelectric and nonlinear optical crystalline material with excellent thermal, chemical, and mechanical stability [1–4], as well as superior ultraviolet–visible (UV–Vis) absorption [5,6]. These characteristics make LT attractive for applications in surface acoustic wave media, optical parametric oscillation device components, and laser gain media, etc. [7–10]. It is known that stoichiometric LT (SLT) possesses fewer crystal structure defects than congruent LT (CLT), and hence exhibits superior properties [11,12] and has attracted significant research interest [13] as a matrix material for optical applications with rare-earth (RE) doping. However, attempts to obtain SLT crystals are hindered by their time-consuming and complex preparation, as well as their high fabricating temperature (1650 °C). Thus, the synthesis of SLT and the investigation of its corresponding properties are worthwhile and pressing challenges. On the other hand, submicron powder (including SLT) could enhance the optical properties like down- and up-conversion and optical amplification [14,15], and has garnered considerable attention owing to its characteristics of convenient preparation, size, and practicality [16,17]. Methods for preparing submicron powder, such as sol-gel, hydrothermal, and soft-chemistry synthesis [18–20], have been extensively investigated. Compared with fabricating bulk single-crystal, previous research has demonstrated that the common problems of long-growth duration and high energy consumption can be overcome. However, the drawback of complex chemical processes, a large number of unwanted byproducts and raw material consumption still exist. Thus, a simple and efficient method for the large-scale synthesis of submicron SLT powders is urgently required.

Rare-earth doped matrix materials have been investigated as a means for the conversion of near-infrared (NIR) laser emissions to visible-light emissions, as well as for the conversion of ultraviolet (UV) to visible light through energy transduction [5,21–24]. Although sulfides and fluorides are the most commonly employed matrix materials for laser conversion [22,25], they still possess the disadvantages of toxicity and poor thermal properties. Specifically, toxic gas SO_2 would be generated due to the reaction between sulfides and oxygen in the air, and the chemical and physical properties of fluorides (including α and β phase) are unstable [26,27]. Above problems impede the large-scale use of sulfide and fluoride host materials. Therefore, the high reliability, environmental-friendliness, low phonon energy, and thermal stability of SLT has rendered it an alternative matrix material [5]. Furthermore, RE^{3+} ions such as Er^{3+}, Dy^{3+}, Tb^{3+}, Eu^{3+}, Sm^{3+}, and Tm^{3+} are commonly employed as activation ions to endow a material with photoluminescence [28–31]. Among these RE^{3+} ions, Er^{3+} ions exhibit a unique electron level structure and abundant energy levels that are frequently used to emit multiband fluorescence. The energy level transitions in Er^{3+} ions allow them to emit NIR fluorescence at a

---

[*] Corresponding author.
[**] Corresponding author. Sino French Institute of Nuclear Engineering and Technology, Sun Yat-sen University, Zhuhai, 519082, China.
E-mail addresses: zhuyzh7@mail.sysu.edu.cn (Y. Zhu), wangbiao@mail.sysu.edu.cn (B. Wang).

https://doi.org/10.1016/j.ceramint.2019.02.146
Received 6 January 2019; Received in revised form 11 February 2019; Accepted 20 February 2019

wavelength of 1.5 μm under 980 nm laser excitation; this waveband is widely exploited in the fields of optical fiber communications, materials processing, and remote sensing. To the best of our knowledge, few studies on the luminescence properties of nanoscale Er^{3+}-doped SLT systems have been reported. Thus, the energy transfer mechanism and potential applications of submicron Er^{3+}-doped SLT powder warrant further study.

In our previous work [32], a modified solid-phase combustion method was used to synthesize pure tantalate submicron powder. This method exploited urea both as a fuel and as an inducer to reduce the temperature and duration of the reaction. In the current study, a series of Er^{3+}-doped SLT powders (xEr:SLT, where x represents the loading of Er^{3+} ions in mol%) were prepared by this method. The crystalline structures, phases, morphologies, and the thermal reaction mechanisms of these powders were investigated using X-ray diffraction (XRD), field-emission scanning electron microscopy (FE-SEM), and thermogravimetric and differential thermal analysis (TG-DTA). Furthermore, the luminescence properties of the xEr:SLT powders under different excitation wavelengths were investigated. Special attention was paid to the visible-region photoluminescence under irradiation with a 980 nm laser, whereby the up-conversion luminescence (UCL) characteristics, including the concentration-dependent spectra, power-dependent spectra, slope of $\log(I_{em})$ *vs.* $\log(P)$, up-conversion mechanism, and decay times were explored. The results indicated that our modified solid-state combustion method, which is efficient, simple, and practical, could be applied to the large-scale production of luminescent RE^{3+}-doped SLT powders. Moreover, these powders exhibit excellent luminescent properties, demonstrating that Er^{3+}-doped SLT submicron particles are a promising material for solid-state lasers and display devices.

2. Materials and methods

Erbium-doped lithium tantalate powders were prepared through a modified solid-state combustion method using the optimum processing parameters (for SLT powder) revealed in our previous study [32]. High-purity (99.99%) Li_2CO_3, Ta_2O_5, Er_2O_3, and urea were mixed with a Li/Ta molar ratio of 1:1, Er^{3+}-doping concentrations of 0.0, 0.5, 1.0, 2.0, and 3.0 mol% (samples a-e), and a urea/(Li_2CO_3 + Ta_2O_5 + Er_2O_3) weight ratio of 3:1. The mixed powders were ground and ball-milled to uniformity, and then heated at 700 °C for 3 h in a muffle furnace.

XRD patterns were obtained at a scanning rate of $0.04\ s{\cdot}step^{-1}$ from 20° to 70° by using a DMAX 2200 VPC X-ray diffractometer. The morphologies and grain sizes of the xEr:$LiTaO_3$ powders were obtained using FE-SEM (JSM-6330F). The thermal reactions of the samples were investigated using Fourier-transform infrared (FT-IR) spectroscopy by means of a simultaneous thermal analysis instrument (STA449F3/Nicolet 6700, Netzsch/ThermoFisher Scientific). The absorption spectra were measured in the 300–1600 nm wavelength region using a Lambda 950 UV–Vis–NIR spectrophotometer (EQUINOX 55, Bruker). Fluorescence emission spectra were recorded using an FLS P980 photoluminescence spectrometer (Edinburgh), equipped with an output-power-tunable 980 nm semiconductor laser as the excitation source. All the fluorescence emission spectra were obtained at room temperature.

3. Results and discussion

3.1. Structure and morphology analysis

The XRD patterns for the xEr:$LiTaO_3$ samples prepared at different doping concentrations are shown in Fig. 1(a). The diffraction peaks are marked with the corresponding lattice planes. All the samples present patterns that match well with pure LT and no impurity peaks can be seen, indicating that Er^{3+}-doping did not change the crystal structure. Because the effective radius of the Er^{3+} ion ($r = 0.88$ Å) is closer to that of the Li^+ ion ($r = 0.76$ Å) than that of the Ta^{5+} ion ($r = 0.64$ Å), considering the ionic radius and the charge balance, the Er^{3+} ion was assumed to occupy the Li^+ sites. In addition, Fig. 1(b) shows the magnifications of the XRD patterns in the range $2\theta = 20–30°$ for various Er^{3+} concentrations. With an increase in the Er^{3+} concentration, the diffraction peaks for the (012) plane shift slightly toward smaller 2θ angles. This could be explained by the lattice volume expansion due to the slightly larger ionic radius of the Er^{3+} ions that occupy the Li sites. The corresponding crystal structure of the LT host (belonging to the space group $R3c$, with cell parameters $a = b = 5.1543$ Å, $c = 13.7835$ Å, and $V = 317.12$ Å^3), and the Er_{Li} structure among oxygen octahedrons ($Ta_{Ta}O_6$) are shown in Fig. 1(c) and (d), respectively.

To study the effects of the Er^{3+} dopant further, FE-SEM was employed to present the particle sizes and morphologies of the doped LT production. As shown in Fig. 2(a)-(d), the four different doping concentration samples (0.5, 1.0, 2.0, and 3.0 mol%) present uniform morphologies and particle sizes. In addition, Li vacancies (V_{Li}) would be generated to maintain the charge balance due to the replacement of Li^+ by Er^{3+} ion with higher valence. The accumulation of vacancies near the grain boundaries can suppress the grain growth [33,34], and therefore, form a more porous structure as shown in Fig. 2(d). Moreover, thin flakes with an average width of 200 nm indicate that the growth speed of nucleation in the (012) plane is the slowest (due to low surface energy for this plane), which is coincident with Pauling's third rule and the Bravais law [35,36]. Thus, we can conclude that the Er^{3+}-dopant influences the as-prepared powders slightly, but the crystalline structure of the submicron xEr:$LiTaO_3$ particles is maintained.

3.2. Thermal reaction analysis

The TG-DTA curve for the raw mixture of *0.5*Er:$LiTaO_3$ was used to analyze the thermal reaction process. The as-prepared samples were heated from room temperature to 700 °C at $3\ °C{\cdot}min^{-1}$. As shown in Fig. 3(a), the TG curve presents two main weight-loss stages comprising 77.09 wt% of the overall weight loss. In the first stage (114–187 °C), the weight loss is 48.03 wt%, which can be ascribed to the decomposition reactions: $CO(NH_2)_2 \rightarrow (CO)_2NH(NH_2)_2 + NH_3$ and $CO(NH_2)_2 \rightarrow C_3N_3(OH)_3 + NH_3$ [32]. The decomposition of urea presents a strong endothermic peak in the DTA curve at 116 °C. Meanwhile, a large amount of gas (NH_3, H_2O, NO_x, etc.) is released and is emitted into the Li_2CO_3, Ta_2O_5, and Er_2O_3 powders. The released gas plays an important role in the second weight loss stage (29.06 wt%), ranging from 187 to 419 °C, which lowers the reaction temperature among the metal oxides by improving the porosity, enhancing the interface reactions, and reducing the bonding energy [32,36]. Specifically, a distinct endothermic peak is observed at 241 °C, which can be attributed to the decomposition of Li_2CO_3. Furthermore, when the temperature is increased from 241 °C to the inflection point (415 °C) in Fig. 3(a), a strong exothermic DTA peak occurs at 321 °C, which may be ascribed to the reaction between metal cations. Thereafter, no evident weight loss is observed above 415 °C, which indicates that the major reactions are complete and that the crystallized rare-earth stoichiometric LT (RE^{3+}-SLT) inorganic phase has been formed. It should be noted the reaction temperature of the submicron RE^{3+}-SLT in this study is much lower than it is in the conventional combustion method, which may be attributed to the reduction in bonding energy induced by the gas penetrating the Li_2O, Ta_2O_5, and Er_2O_3. Thus, we can conclude that the urea takes part in the reaction, improves porosity, and greatly enhances interfacial reactions.

3.3. Photoluminescence properties

The room-temperature absorption spectra of the different xEr:SLT samples in the UV–Vis and NIR regions were recorded and are presented in Fig. 3(b) and (c). As expected, no absorption peak was observed in the undoped SLT, whereas eight evident peaks were observed

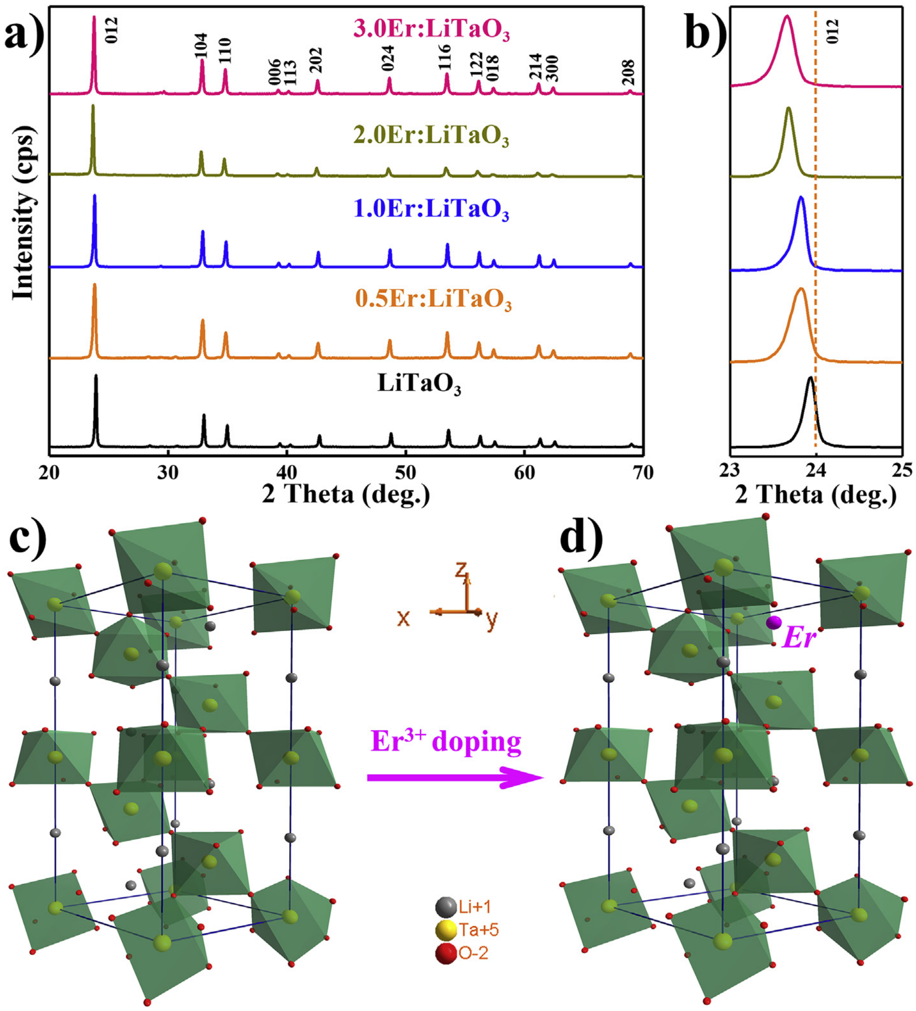

Fig. 1. (a) XRD patterns of the prepared samples at different doping concentrations of Er^{3+} ions. (b) Magnified XRD patterns along the (012) plane of xEr:$LiTaO_3$. (c, d) The crystal structures of xEr:$LiTaO_3$.

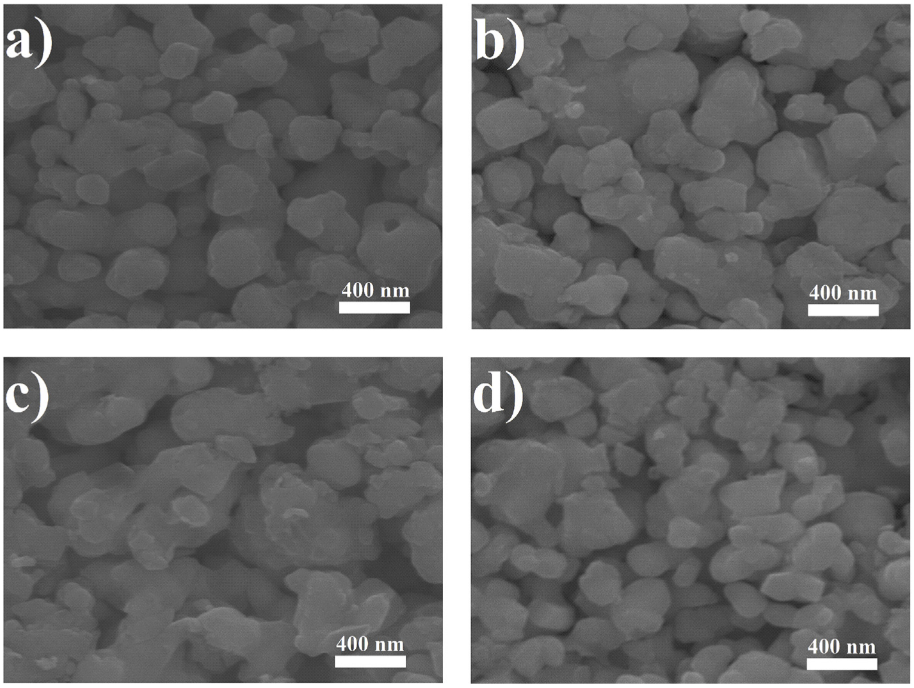

Fig. 2. Micrographs of xEr:$LiTaO_3$ powder with different Er^{3+} doping concentrations (a) 0.5 mol%, (b) 1.0 mol%, (c) 2.0 mol%, and (d) 3.0 mol%.

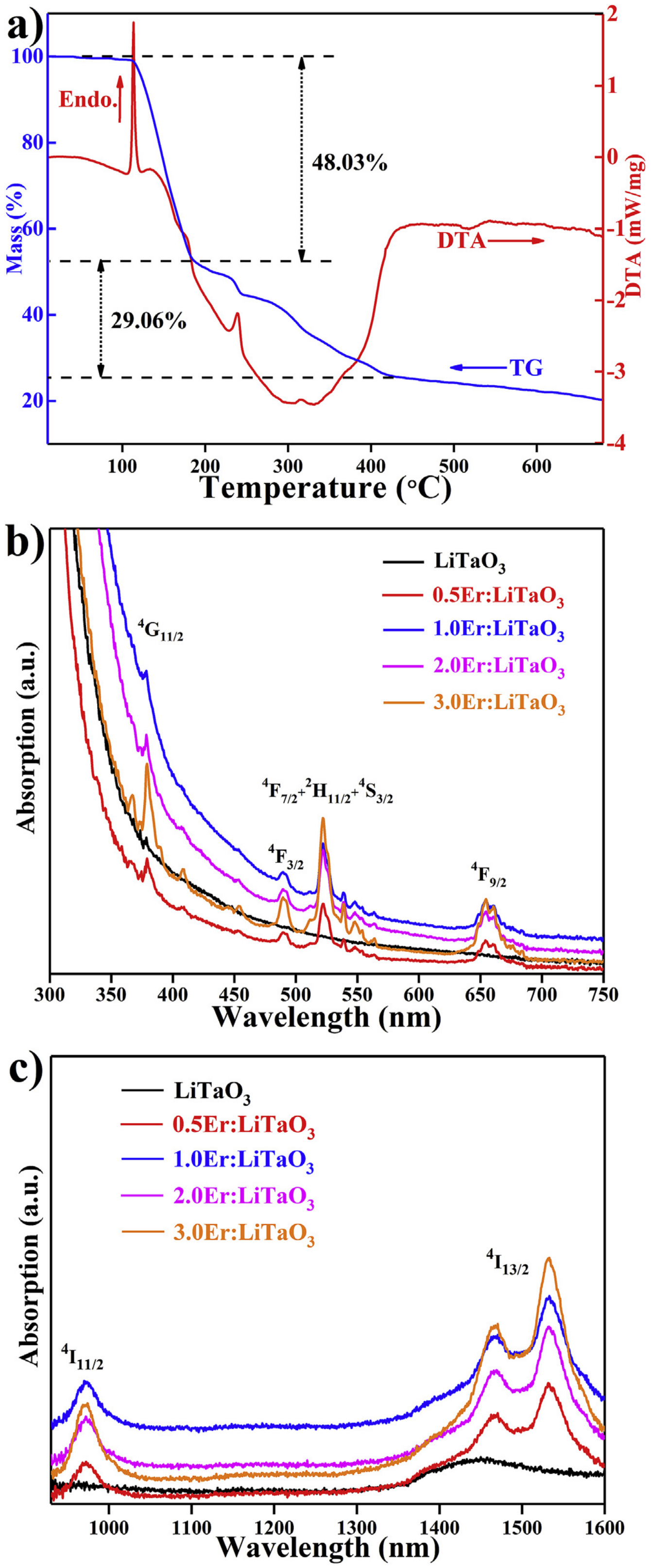

Fig. 3. (a) TG-DTA curves of the raw mixture powder under temperatures increasing from room temperature to 700 °C. (c, d) UV–Vis and NIR absorption spectra of xEr:LiTaO$_3$ crystals, respectively.

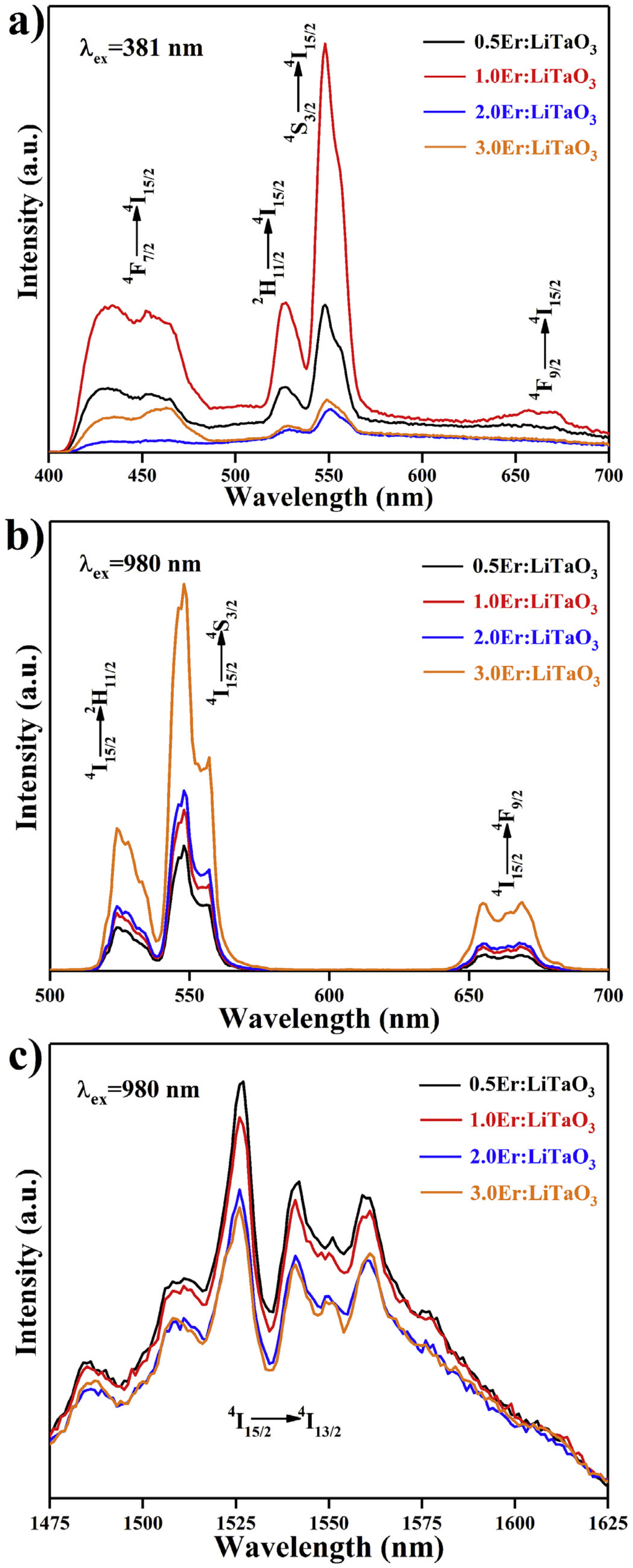

Fig. 4. (a) The fluorescence emission spectra of xEr:LiTaO$_3$ under 381 nm laser excitation. (b) Visible fluorescence emission spectra, and (c) near infrared fluorescence emission spectra of xEr:LiTaO$_3$ under 980 nm laser excitation.

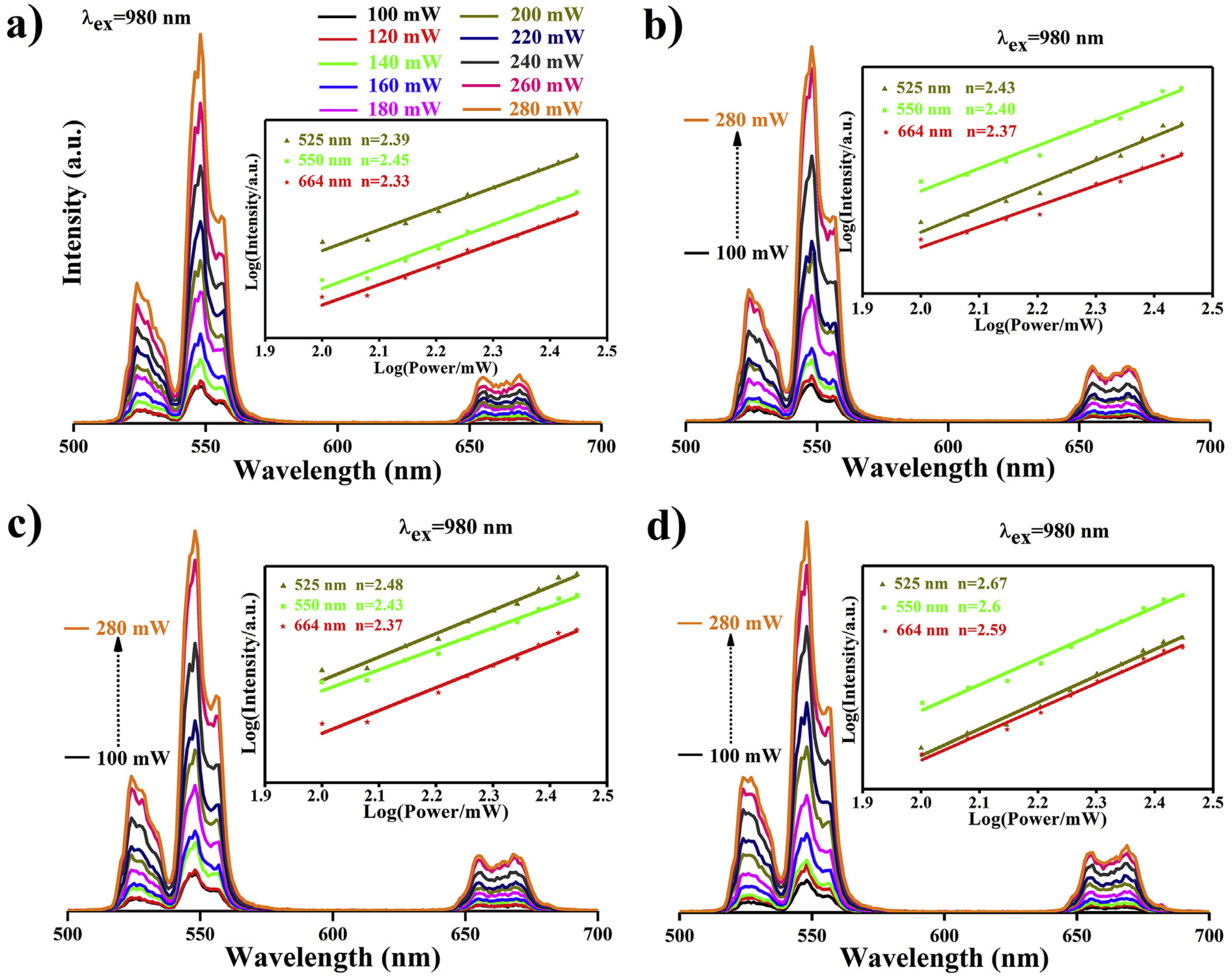

Fig. 5. UCL spectra of the as-prepared (a) *0.5*Er:LiTaO$_3$, (b) *1.0*Er:LiTaO$_3$, (c) *2.0*Er:LiTaO$_3$, and (d) *3.0*Er:LiTaO$_3$ samples under 980 nm laser excitation in different pumping powers. The insets present the corresponding power dependence of the UCL process.

in the Er^{3+}-doped systems. The absorption peaks correspond to transitions from the ground state ($^4I_{15/2}$) to the excited states of Er^{3+} ($^4G_{11/2}$, $^4F_{3/2}$, $^4F_{7/2}$, $^2H_{11/2}$, $^4S_{3/2}$, $^4F_{9/2}$, $^4I_{9/2}$, $^4I_{11/2}$, and $^4I_{13/2}$), as indicated in Fig. 3(b) and (c). The strong absorptions around 381 and 980 nm are commonly selected as excitation sources for multicolor DCL and UCL luminescence emissions, respectively. The fixed-emission spectra will be presented in the following sections. In addition, the UV–Vis–NIR absorption bands centered at 525, 550, 658, and 1540 nm are attributable to the Er^{3+} transitions, i.e., $^4I_{15/2} \rightarrow {}^4F_{7/2}$, $^2H_{11/2}$, $^4S_{3/2}$, $^4F_{9/2}$, and $^4I_{13/2}$, respectively.

The fluorescence emission spectra of the *x*Er:LiTaO$_3$ samples recorded under the 381 and 980 nm pump laser excitation are presented in Fig. 4. Specifically, in the DCL spectra in Fig. 4(a), three emission peaks centered at 550, 525, and 658 nm, and a broad emission band between 410 and 490 nm can be seen, which correspond to the energy transfer from $^4S_{3/2}$, $^2H_{11/2}$, $^4F_{9/2}$, and $^4F_{7/2}$ to $^4I_{15/2}$, respectively. The emission intensity for green light centered at 550 nm is stronger than that for the other green emission (centered at 525 nm) and the blue emission (ranging between 410 and 490 nm), with the weakest emission being that of red light (centered at 658 nm). Furthermore, the intensities of the red emissions are extremely weak when the doping concentrations of Er^{3+} are 2.0 and 3.0 mol%. This phenomenon can be ascribed to the multi-phonon relaxation process that occurs between the $^4G_{11/2}$ and the $^4S_{3/2}$ and $^2H_{11/2}$ states after the Er^{3+} ions are excited to the $^4G_{11/2}$ state under 381 nm excitation. In addition, the intensities of the multicolor emission spectra are enhanced with an increase in the concentration of Er^{3+} from 0.5 to 1.0 mol%. Furthermore, when the concentration reaches 2.0 and 3.0 mol%, the emission intensities decrease sharply, which could be explained by the occurrence of concentration quenching.

The UC emission spectra of Er^{3+}-doped SLT phosphors at different concentrations under 980 nm excitation are shown in Fig. 4(b) and (c). We can observe an extremely strong green emission (centered at 550 nm), a relatively weak blue-green emission (centered at 525 nm), a weak red emission (ranging between 590 and 675 nm), and an NIR emission (centered at 1.5 μm), which correspond to the transitions of Er^{3+} ions from the ground state $^4I_{15/2}$ to the excited states $^4S_{3/2}$, $^2H_{11/2}$, $^4F_{9/2}$, and $^4I_{13/2}$, respectively. Moreover, as can be seen from Fig. 4(b) and (c), the luminescence intensity significantly changes with the increase in Er^{3+} ion concentration, and the optimal concentrations are 3.0 and 0.5 mol% for visible and NIR emissions, respectively. Notably, concentration quenching does not occur for UCL in visible emissions, which illustrates that a higher concentration of Er^{3+}-dopant in the SLT system can be applied. Furthermore, the shapes of the fluorescence spectra are maintained, which implies that the stable crystal field around the Er^{3+} ion does not change with a dopant concentration of 3.0 mol%.

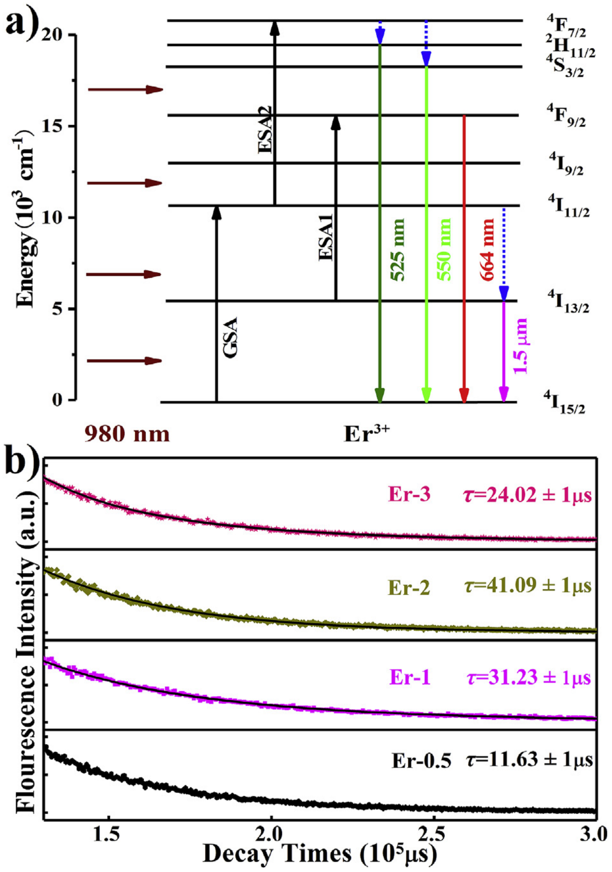

Fig. 6. (a) Energy level diagram of the up-conversion mechanism of Er:LiTaO$_3$ samples. (b) Decay curves for *x*Er:LiTaO$_3$ samples monitored at 550 nm emission.

3.4. Energy transfer mechanism

Previous research [37] has indicated that the DCL mechanism can be explained simply as electrons repopulating from specific higher energy states to certain low energy states, accompanied by emission. However, because the excited electron can populate in different ways, the UCL mechanism is rather complex, and thus worthy of in-depth investigation [37,38]. The UCL mechanism of the *x*Er:LiTaO$_3$ system has been studied in detail. Specifically, in the unsaturated UCL process, the relationship between the emission light intensity (I_{em}) and the pump laser power (P) of the excitation resource is expressed as:

$$I_{em} \propto P^n \tag{1}$$

where n is the number of photons absorbed in the UCL process.

The UCL spectra of the *x*Er:LiTaO$_3$ powders under 980 nm excitation at different pump powers are shown in Fig. 5. All these spectra are similar in shape, and the emission intensity increases with the pump power. The number of absorbed photons is calculated by the ratio of log I_{em} to log P. Accordingly, the data for the 525 nm (Er: $^4I_{15/2} \rightarrow {}^2H_{11/2}$), 550 nm (Er: $^4I_{15/2} \rightarrow {}^4S_{3/2}$), and 664 nm (Er: $^4I_{15/2} \rightarrow {}^4F_{9/2}$) transitions were plotted, and the fitted results are presented in the insets of Fig. 5. Specifically, for the *0.5*Er:LiTaO$_3$ system, the values of the slopes for the $^4I_{15/2} \rightarrow {}^2H_{11/2}$, $^4I_{15/2} \rightarrow {}^4S_{3/2}$, and $^4I_{15/2} \rightarrow {}^4F_{9/2}$ transitions are 2.39, 2.45, and 2.33, respectively. In addition, the slopes of other samples present similar results, namely n values are maintained between 2 and 3. Due to energy relaxation, the emitted energy is lower than the absorbed energy, leading to the slope values being less than 3 [39,40]. Thus, we can conclude that three photons are absorbed in the UCL process.

UCL processes may proceed according to three types of luminescence mechanisms: ground/excited state absorption (GSA/ESA), photon avalanche (PA), and energy transfer (ET) [39]. Based on the above analysis, the likely UC mechanisms are discussed in terms of the energy levels illustrated in Fig. 6(a). In this energy level diagram, the green, red, and black solid arrows represent the emission and multiphonon processes, and the blue dotted arrows represent the energy relaxation process. As shown in Fig. 6(a), the excited electron in the ground state ($^4I_{15/2}$) is excited to the $^4I_{11/2}$ state through GSA when an Er^{3+} ion absorbs a photon from the NIR laser. Simultaneously, some electrons in the $^4I_{11/2}$ state relax rapidly and non-radiatively to the lower level $^4I_{13/2}$. Therefore, at the $^4I_{13/2}$ state, electrons that populate to the $^4F_{9/2}$ state are the consequence of the ESA1 process, and the ones that transfer to the $^4I_{15/2}$ state with the NIR emission ($^4I_{13/2} \rightarrow {}^4I_{15/2}$) at 1.5 μm could be explained as the energy relaxation. After that, the electrons in the excited state return to the ground state by radiative transition and generate red emission ($^4F_{9/2} \rightarrow {}^4I_{15/2}$) at 664 nm. Alternatively, under the effect of the ESA2 mechanism, the excited electrons at the $^4I_{11/2}$ energy level are excited to a higher energy level ($^4F_{7/2}$). As energy relaxation occurs, the electrons jump from $^4F_{7/2}$ to the $^2H_{11/2}$ and $^4S_{3/2}$ states. Thus, a bright green emission ($^2H_{11/2}$, $^4S_{3/2} \rightarrow {}^4I_{15/2}$) occurs at 525/550 nm, and the excited electrons return to the ground state.

3.5. Luminescence decay

The luminescence decay measurements for the $^4S_{3/2} \rightarrow {}^4I_{15/2}$ (550 nm) transition under 980 nm excitation are presented in Fig. 6(b). According to previous research [41], fluorescence lifetime can be fitted with the double-exponential formula,

$$I(\tau) = I_0 + A_1 \exp(-t/\tau_1) + A_2 \exp(-t/\tau_2) \tag{2}$$

where $I(\tau)$ represent the fluorescence intensity at time t, I_0 represents the background light intensity (set to zero), τ_1 and τ_2 are the shorter and longer lifetimes, A_1 and A_2 are the weight factors. Based on the above parameters, the decay time can be calculated by the formula,

$$\tau = (A_1\tau_1^2 + A_2\tau_2^2)/(A_1\tau_1 + A_2\tau_2) \tag{3}$$

As shown in Fig. 6(b), the fluorescence lifetimes of the doped samples were calculated to be 11.63, 31.23, 41.09, and 24.02 μs, respectively. The fluorescence lifetime changes drastically with the Er^{3+} ion concentration. This can be explained by the occupation of different sites and radiation trapping [42–44]. However, the lifetime sharply decreases when Er^{3+} concentration exceeds 2.0 mol%, which is due to concentration quenching. In addition, the host defects and the interactions between RE^{3+} ions lead to a sharp decrease in the fluorescence lifetime [45,46]. These results show that the concentration of Er^{3+} ions significantly affects the fluorescence lifetime, and that the optimal doping concentration is 2.0 mol%.

4. Conclusions

A series of submicron Er^{3+}-doped SLT particles were synthesized by a modified solid-state combustion method. The particles were then studied by means of XRD and SEM, which revealed that all the *x*Er:LiTaO$_3$ samples had similar crystalline structures, grain sizes, and morphologies. TG-DTA revealed that urea, reducing reaction temperature and shortening reaction time, acted as both a fuel and an inducer. Notably, this method is efficient, simple, and practical, and could be used to synthesize submicron RE^{3+}-doped SLT particles, or conveniently applied to the synthesis of other doped polycrystalline particles. More importantly, the as-prepared samples presented intense photoluminescence. Specifically, in the DCL and UCL processes, the intensity of the emission varies with the dopant concentration. The optimal concentrations for DCL and UCL are 1.0 and 3.0 mol%, respectively, in the visible region. However, for NIR emissions, the optimal concentration is 0.5 mol%. Furthermore, the power-dependent

UCL spectra for xEr:$LiTaO_3$ revealed a three-photon absorption process, indicating more intense absorption and emission processes than common Er-doped crystalline materials. By analyzing this multi-photon absorption mechanism, the corresponding energy level diagram was provided. Fluorescence lifetimes were significantly influenced by the concentration of Er^{3+} ions.

In sum, Er:$LiTaO_3$ submicron powders with excellent photoluminescent properties were synthesized by a modified solid-state combustion method, which presents practical value for the large-scale industrial production of RE^{3+}-doped phosphors. In addition, the excellent photoluminescence properties of the Er^{3+}-doped SLT phosphors demonstrate their potential for solid-state lasers, optical fiber communications, and displays.

Acknowledgments

This work was supported by the National Natural Science Foundation of China (NSFC) (No. 51802358, 11832019, 11372361), the National Natural Science Foundation of Guangdong Province (2018A030313321, 2017A030310426), the Guangdong Science & Technology Project (2015B090927005) and the Fundamental Research Funds for the Central Universities (17lgpy37).

References

[1] V.Ya. Shur, A.R. Akhmatkhanov, D.S. Chezganov, A.I. Lobov, I.S. Baturin, M.M. Smirnov, Shape of isolated domains in lithium tantalate single crystals at elevated temperatures, Appl. Phys. Lett. 103 (2013) 242903.

[2] L.L. Xing, Y.L. Xu, R. Wang, W. Xu, Influence of temperature on upconversion multicolor luminescence in $Ho^{3+}/Yb^{3+}/Tm^{3+}$-doped $LiNbO_3$ single crystal, Opt. Lett. 14 (2013) 2535–2537.

[3] F. Juvalta, M. Jazbinšek, P. Günter, K. Kitamura, Electro - optical properties of near - stoichiometric and congruent lithium tantalate at ultraviolet wavelengths, J. Opt. Soc. Am. B 23 (2006) 276–281.

[4] N. Masaru, S. Takekawa, K. Kitamura, Anisotropy of thermal conductivities in non- and Mg-doped near-stoichiometric $LiTaO_3$ crystals, Opt. Mater. 32 (2010) 1410–1412.

[5] P. Gȕnter, J.P. Huignard, Photorefractive Materials and Their Applications 2, optical sciences springer press, 2006.

[6] A. Ashkin, G.D. Boyd, J.M. Dziedzic, R.G. Smith, A.A. Ballman, J.J. Levinstein, K. Nassau, Optically-induced refractive index inhomogeneities in $LiNbO_3$ and $LiTaO_3$, Appl. Phys. Lett. 9 (1966) 72–74.

[7] A.M. Glass, R.L. Abrams, Study of piezoelectric oscillations in wideband pyroelectric $LiTaO_3$ detectors, J. Appl. Phys. 41 (1970) 4455–4459.

[8] R. Rimeika, J. Belovickis, D. Čiplys, Leaky-surface-wave generated acoustic beam displacement upon reflection in lithium tantalate crystals, Appl. Phys. Lett. 102 (2013) 03160101–03160104.

[9] N.E. Yu, S. Kurimura, Y. Nomura, M. Nakamura, K. Kitamura, J. Sakuma, Y. Otani, A. Shiratori, Periodically poled near-stoichiometric lithium tantalate for optical parametric oscillation, Appl. Phys. Lett. 84 (2004) 1662–1664.

[10] Y. Liu, K. Kitamura, S. Takekawa, M. Nakamura, Y. Furukawa, H. Hatano, Nonvolatile two-color holographic recording in nondoped near-stoichiometric lithium tantalate crystals with continuous-wave lasers, Appl. Phys. Lett. 82 (2003) 4218–4220.

[11] Y.N. Qian, B. Wang, R. Wang, L.L. Xing, Y.L. Xu, Upconversion emission in near-stoichiometric $LiNbO_3$:Er^{3+} crystal, RSC Adv. 3 (2013) 13507–13514.

[12] Y.X. Fan, Z.M. Yu, W.H. Li, C. Xu, K. Fu, Enhancement of blue holographic properties in Zr^{4+}-doped near stoichiometric Fe:$LiNbO_3$ crystals, Optic Laser. Technol. 244 (2012) 362–365.

[13] P.C. Hu, Y. Hang, R. Li, J. Gong, J.G. Yin, C.C. Zhao, X.M. He, T. Yu, L.H. Zhang, W.B. Chen, Y.Y. Zhu, 1.083 μm laser operation in Nd,Mg:$LiTaO_3$ crystal, Laser Phys. Lett. 8 (10) (2011) 710–714.

[14] J.J. Schuyt, G.V.M. Williams, Photoluminescence, radioluminescence and optically stimulated luminescence in nanoparticle and bulk $KMgF_3$(Eu), J. Lumin. 204 (2018) 472–479.

[15] M. Wu, E.H. Song, Z.T. Chen, S. Ding, S. Ye, J.J. Zhou, S.Q. Xu, Q.Y. Zhang, Single-band red upconversion luminescence of Yb^{3+}-Er^{3+} via nonequivalent substitution in perovskite $KMgF_3$ nanocrystals, J. Mater. Chem. C 4 (2016) 1675–1684.

[16] G.Y. Chen, I. Roy, C. Yang, P.N. Prasad, Nanochemistry and nanomedicine for nanoparticle- based diagnostics and therapy, Chem. Rev. 116 (2016) 2826–2885.

[17] Z.X. Li, J.C. Barnes, A. Bosoy, J.F. Stoddart, J.I. Zink, Mesoporous silica nanoparticles in biomedical applications, Chem. Soc. Rev. 41 (2012) 2590–2605.

[18] M.Y. Ding, C.H. Lu, L. Chen, W.F. Bai, Y.J. Yuan, Z.G. Ji, Transparent sol-gel glass ceramics containing β-$NaYF_4$:Yb^{3+}/Er^{3+} nanocrystals: structure, upconversion luminescent properties and optical thermometry behavior, Ceram. Int. 44 (2018) 16379–16387.

[19] A.I. Ramos-Guerra, I. Martínez-Merlín, C. Falcony, The role of the stabilizing agent on the structural and luminescent properties of hydrothermally synthesized ZrO_2:Tb^{3+} phosphors, Ceram. Int. 44 (2018) 13744–13749.

[20] M.N. Liu, D.F. Xue, K.Y. Li, Soft-chemistry synthesis of $LiNbO_3$ crystallites, J. Alloy. Comp. 449 (2008) 28–31.

[21] J.K. Cao, D.K. Xu, F.F. Hu, X.M. Li, W.P. Chen, L.P. Chen, Transparent $Sr_{0.84}Lu_{0.16}F_{2.16}$: Yb^{3+}, Er^{3+} glass ceramics: elaboration, structure, up-conversion properties and applications, J. Eur. Ceram. Soc. 38 (2018) 2753–2758.

[22] Y. Fei, S.L. Zhao, X. Sun, L.H. Huang, D.G. Deng, S.Q. Xu, Preparation and optical properties of Eu^{3+} doped and Er^{3+}/Yb^{3+} codoped oxyfluoride glass ceramics containing $Ba_{1-x}Lu_xF_{2+x}$ nanocrystals, J. Non-Cryst. Solids 428 (2015) 20–25.

[23] X.M. Yin, H. Wang, M.M. Xing, Y. Fu, Y. Tian, T. Jing, X.X. Luo, High color purity red emission of $Y_2Ti_2O_7$:Yb^{3+}, Er^{3+} under 1550 and 980 nm excitation, J. Lumin. 182 (2017) 183–188.

[24] Y.N. Qian, R. Wang, B. Wang, C. Xu, W. Xu, L.L. Xing, Y.L. Xu, Optical characteristics of Er^{3+} ion in Er/Yb:$LiNbO_3$ crystal: comparison with the dissimilar effect of anti-photorefractive ions Zn^{2+}, In^{3+} and Zr^{4+}, J. Quant. Spectrosc. Radiat. Transfer 129 (2013) 60–68.

[25] R.-J. Xie, N. Hirosaki, Silicon-based oxynitride and nitride phosphors for white LEDs-A review, Sci. Technol. Adv. Mater. 8 (2007) 588–600.

[26] J.B. Lian, F. L, X.J. Wang, X.D. Sun, Hydrothermal synthesis and photoluminescence properties of $Gd_2O_2SO_4$:Eu^{3+} spherical phosphor, Powder Technol. 253 (2014) 187–192.

[27] L.Z. Zhang, Y.S. Huang, S.J. Sun, F.F. Yuan, Z.B. Lin, G.F. Wang, Thermal and spectral characterization of Cr^{3+}:$MgWO_4$-a promising tunable laser material, J. Lumin. 169 (2016) 161–164.

[28] X. Qiao, X. Fan, J. Wang, M. Wang, Luminescence behavior of Er^{3+} ions in glass-ceramics containing CaF_2 nanocrystals, J. Non-Cryst. Solids 351 (2005) 357–363.

[29] S.W. Long, D.C. Ma, Y.Z. Zhu, M.M. Yang, S.P. Lin, B. Wang, Temperature dependence of white light emission and energy transfer in Dy^{3+} and Tm^{3+} co-doped $LiNbO_3$ single crystals, J. Lumin. 192 (2017) 728–733.

[30] Z.G. Cui, R.G. Ye, D.G. Deng, Y.J. Hua, S.L. Zhao, G.H. Jia, C.X. Li, S.Q. Xu, Eu^{2+}/Sm^{3+} ions co-doped white light luminescence $SrSiO_3$ glass-ceramics phosphor for White LED, J. Alloy. Comp. 509 (2011) 3553–3558.

[31] S.W. Long, D.C. Ma, Y.Z. Zhu, M.M. Yang, S.P. Lin, B. Wang, Effects of Zr^{4+} co-doping on the spectroscopic properties and yellow light emissions of Dy^{3+} in $LiNbO_3$ single crystals, Opt. Mater. Express 6 (2016) 3354–3364.

[32] Y.Z. Zhu, S.P. Lin, Y. Liu, D.C. Ma, B. Wang, Efficient synthesis of stoichiometric lithium tantalate powder by a solid-state combustion route, Mater. Manuf. process. 30 (2015) 1342–1347.

[33] D. Gao, K.W. Kwok, D. Lin, H.L.W. Chan, Microstructure and electrical properties of La-modified $K_{0.5}Na_{0.5}NbO_3$ lead-free piezoelectric ceramics, J. Phys. D Appl. Phys. 42 (2009) 035411-1-6.

[34] J.F. Lin, J. Xu, C.W. Liu, Y.H. Lin, X. Wu, C. Lin, X.H. Zhen, C. Chen, Effects of compositional changes on up-conversion photoluminescence and electrical properties of lead-free Er-doped $K_{0.5}Na_{0.5}NbO_3$-$SrTiO_3$ transparent ceramics, J. Alloy. Comp. 784 (2019) 60–67.

[35] M. Liu, D. Xue, C. Luo, Facile synthesis of lithium niobite squares by a combustion route, J. Am. Ceram. Soc. 89 (2006) 1551–1556.

[36] M. Liu, D. Xue, An efficient approach for the direct synthesis of lithium niobite powders, Solid State Ionics 177 (2006) 275–280.

[37] Z. Liang, E.W. Sun, Z.Y. Liu, Z.G. Zhang, J.T. Zeng, W. Ruan, G.R. Li, W.W. Cao, Electric field induced upconversion fluorescence enhancement and its mechanism in Er^{3+} doped $0.75Pb(Mg_{1/3}Nb_{2/3})O_3$-$0.25PbTiO_3$ transparent ceramic, Appl. Phys. Lett. 109 (2016) 132904-1-4.

[38] F. Auzel, Upconversion and anti-Stokes processes with f and d ions in solids, Chem. Rev. 104 (2004) 139–173.

[39] H.N. Huang, H.F. Zhou, J. Zhou, T. Wang, D. Huang, D.P. Huang, Y.Q. Wu, L.L. Sun, G.J. Zhou, J. Zhan, J.F. Hu, Enhanced anti-stocks luminescence in $LaNbO_4$:Ln^{3+} (Ln^{3+} $=Yb^{3+}$, $Er^{3+}/Ho^{3+}/Tm^{3+}$) with abundant color, RSC Adv. 7 (2017) 16777–16786.

[40] M. Pollnau, D.R. Gamelin, S.R. Lüthi, H.U. Güdel, M.P. Hehlen, Power dependence of upconversion luminescence in lanthanide and transition-metal-ion systems, Phys. Rev. B 61 (2000) 3337–3346.

[41] H.X. Zhang, C.H. Kam, Y. Zhou, X.Q. Han, S. Buddhudu, Q. Xiang, Y.L. Lam, Y.C. Chan, Green upconversion luminescence in Er^{3+}:$BaTiO_3$ films, Appl. Phys. Lett. 77 (2000) 609–611.

[42] P. Babu, H.J. Seo, K.H. Jang, R. Balakrishnaiah, C.K. Jayasankar, A.S. Joshi, Optical spectroscopy and energy transfer in Tm^{3+} doped metaphosphate laser glasses, J. Phys. Condens. Matter 17 (2005) 4859–4876.

[43] S.X. Shen, M. Naftaly, A. Jha, Tungsten-tellurite - a host glass for broadband EDFA, Optic Commun. 205 (2002) 101–105.

[44] K. Venkata Krishnaiah, J. Marques-Hueso, K. Suresh, G. Venkataiah, B.S. Richards, C.K. Jayasankar, Spectroscopy and near infrared upconversion of Er^{3+}-doped TZNT glasses, J. Lumin. 169 (2016) 270–276.

[45] L.R.P. Kassab, L.C. Courrol, R. Seragioli, N.U. Wetter, S.H. Tatumi, L. Gomes, Er^{3+} laser transition in PbO-PbF_2-B_2O_3 glasses, J. Non-Cryst. Solids 348 (2004) 94–97.

[46] E. Cervantes-Juárez, A.N. Meza-Rocha, W. Romero-Romo, U. Caldiño, C. Falcony, E. Álvarez, M. Palomino-Ovando, R. Lozada-Morales, Up and down-shifting emission properties of novel Er^{3+}-doped CdO-V_2O_5-P_2O_5 glass system, Ceram. Int. 45 (2019) 1609–1615.